Comparative study on photocatalytic degradation of Congo red using different clay mineral/CdS nanocomposites

Xiaowen Wang[1,2,3] · Bin Mu[1,3] · Aiping Hui[1,3] · Aiqin Wang[1,3]

Abstract

Clay mineral/CdS nanocomposites were successfully prepared via hydrothermal technique in the presence of different clay minerals for photocatalytic degradation of Congo red. The relevant structures and properties were systematically characterized and studied, including phase composition, crystal size, color, optical property and morphology of the obtained nanocomposites. The generated hexagonal CdS nanoparticles with a diameter of 30–60 nm were well anchored on the surface of clay minerals. Interestingly, the types of clay minerals affected the UV–Vis absorbance and band-gap energy of clay mineral/CdS nanocomposites, and the clay mineral/CdS nanocomposites derived from one-dimensional halloysite, sepiolite, and palygorskite exhibited higher photocatalytic activity for Congo red degradation than that of two-dimensional lamellar kaolin and montmorillonite. In addition, incorporating of clay minerals not only effectively decreased the size of CdS nanoparticles without the obvious aggregation, but also guard against electrochemical corrosion of CdS during photocatalytic degradation.

1 Introduction

The immoderate discharge of large amount of industrial colored wastewater containing various dyes seriously caused environmental pollution and threatened our public health and living conditions [1, 2]. Although many laws and stringent regulations have been established to control and restrict the illegal discharge behavior, it is very necessary to remove or degrade dyes to reach allowable levels [3]. To date, various

✉ Bin Mu
mubin@licp.cas.cn

✉ Aiqin Wang
aqwang@licp.cas.cn

1 Key Laboratory of Clay Mineral Applied Research of Gansu Province, Center of Eco-Materials and Green Chemistry, Lanzhou Institute of Chemical Physics, Chinese Academy of Sciences, Lanzhou 730000, People's Republic of China

2 Center of Materials Science and Optoelectronics Engineering, University of Chinese Academy of Sciences, Beijing 100049, People's Republic of China

3 Center of Xuyi Palygorskite Applied Technology, Lanzhou Institute of Chemical Physics, Chinese Academy of Sciences, Xuyi 211700, People's Republic of China

methods have been successfully developed to remove or degrade dyes in wastewater, such as membrane separation [4], photocatalytic degradation [5], adsorption [6], chemical oxidation, etc. [7]. Among them, photocatalytic degradation has been proven to be a reliable and promising water treatment technology to degrade organic dye pollutants [8].

Owing to low-cost, narrow band gap (2.42 eV), stable and high photocatalytic activity, CdS as a promising photocatalyst has attracted wide interest in the past two decades in the energy and environment fields [9, 10]. However, the aggregation of CdS nanoparticles and recombination of photoexcited charge carriers of CdS resulted in decreasing in photocatalytic activity during photocatalytic process. To address these issues, it was found that incorporation of carriers could effectively resolve aggregation, and improve the photocatalytic activity and stability of CdS nanoparticles [11], and the common carriers included carbon nanotubes [12], graphitic [13], metals (Ag or Au) [14], porous materials [15], etc. However, these supporters are expensive, and the involved preparation process of them is complicated. By contrast, natural clay minerals are recognized as promising carriers for loading of CdS nanoparticles, e.g., natural laponite [16], montmorillonite (Mt) [17, 18], kaolin (K) [19, 20], halloysite nanotubes (HNTs) [21] and palygorskite (Pal) [22, 23]. Although there are many reports related to clay mineral/CdS nanocomposites, few attentions have been paid to the effect of different clay minerals on photocatalytic

activity of clay mineral/CdS nanocomposites to our knowledge. Moreover, photocatalytic dye degradation are mainly focused on the cationic dyes (Rhodamine B [24], methylene blue [23]), and it hardly investigates their photocatalytic degradation behavior toward anionic dyes.

According to early reports, the types of clay minerals influenced the optical properties of clay mineral/CdS nanocomposites [25], which further resulted in the difference in their band-gap energy. Our previous work also revealed the relationship between the color and photocatalytic property of Pal/CdS nanocomposites [26]. In this work, different clay minerals were employed to fabricate clay mineral/CdS nanocomposites for photocatalytic degradation of anionic dye of Congo red (CR) including Mt, K, HNTs, Sepiolite (Sep) and Pal. Crystalline structure, color and morphology of the as-prepared clay mineral/CdS nanocomposites were characterized and analyzed in detail, and their photocatalytic degradation properties to CR were also comparatively studied.

2 Experimental section

2.1 Materials and reagents

Pal, HNTs, K, Sep and Mt were obtained from Jiuchuan Clay Technology Co. Ltd (Jiangsu, China), Zhengzhou Las Vegas Sun Ceramics Co., Ltd (Henan, China), Long Yan Kaolin Clay Co., Ltd (Fujian, China), Yixian Dazhi Thermal Insulation Materials Co., Ltd (Hebei, China), and Inner Mongolia Ningcheng Chemical Co., Ltd (China), respectively. Before being used, these clay minerals were treated using 2 wt% sulfuric acid at room temperature for 4 h. Thiourea (NH_2CSNH_2) and cadmium chloride hydrate ($CdCl_2 \cdot 2.5H_2O$) were purchased from Tianjin Kemiou Chemical Reagent Co., Ltd and Shanghai Sanyou Reagent Factory, respectively. CR was provided from Tianjin Kemiou Chemical Reagent Co., Ltd (Tianjin, China). Above reagents were all of analytical grade without the further purification, and the distilled water was used in preparation of all solutions.

2.2 Preparation of clay mineral/CdS nanocomposite

Clay mineral/CdS nanocomposites were facilely prepared *via* an effective and safe hydrothermal decomposition of $[Cd(NH_2CSNH_2)_2]Cl_2$ in the presence of clay minerals [26]. Briefly, clay minerals (1.50 g) were added into 50.0 mL water by vigorous magnetic stirring for 30 min to obtain suspension, and then $CdCl_2 \cdot 2.5H_2O$ and NH_2CSNH_2 with a molar ratio of 1:1 were dissolved into 15 mL water to form the white complex precursor. After that, the precursor was dropped into suspension under stirring. The final obtained solutions were then transferred into a Teflon-lined stainless steel autoclave with a capacity of 100 mL followed by a hydrothermal treatment at 180 °C for 6 h. After this process, the precipitates were separated by centrifugation, and subsequently washed with water and ethanol several times before being dried at 60 °C for 24 h. For comparison, pure CdS without clay minerals was also prepared by the same procedures. The serial numbers of the as-prepared samples were presented in Table 1, and schematic illustration of the preparation process of clay mineral/CdS nanocomposites was presented in Fig. 1. Due to the small size and high positive charge of the organic $Cd[NH_2CSNH_2]_2Cl_2$ complex, electrostatic interaction is the predominant driving force for loading of CdS nanoparticles in this system.

2.3 Measurement of photocatalytic activity

The photocatalytic activity of clay mineral/CdS nanocomposites was evaluated by photo degradation of CR at room temperature. The reaction was carried out in GHX-2 photocatalytic reactor under 300 W xenon lamp (providing visible light ≥ 400 nm). 30 mg nanocomposites were suspended in 50 mL CR solution (30 mg/L), the reaction systems was kept in the dark with magnetic stirring for 30 min to reach absorption equilibrium. Next, the xenon lamp was placed 10 cm above photocatalytic reactor to simulate visible light. Sample aliquots of about 4 mL were collected with a disposable syringe at every 10 min intervals and immediately filtered using 0.22 μm of filter head to completely remove

Table 1 Hexagonal lattice parameters (*a, b, c, V* and *β*), rietveld refinement results, zeta potential and BET surface areas of the samples

Samples	Cystallite size (nm)	Cell parameters		Cell volume ($Å^3$)	Zeta potential (eV)	BET surface areas (m^2/g)
		$a = b$ (Å)	c (Å)			
HNTs/CdS	46.5307	4.12130	6.70100	98.8799	− 22.47	45.2549
K/CdS	51.7989	4.14140	6.71005	99.6783	− 20.60	10.8548
Sep/CdS	34.8239	4.14753	6.72065	100.1315	− 24.77	16.9579
Mt/CdS	44.4689	4.13900	6.71610	99.6526	− 37.17	65.5556
Pal/CdS [26]	57.4854	4.13999	6.71459	99.6779	− 31.17	97.0834
CdS [26]	80.3623	4.12551	6.70100	98.7815	− 17.00	7.6719

Fig. 1 Schematic illustration of preparation of clay mineral/CdS nanocomposites
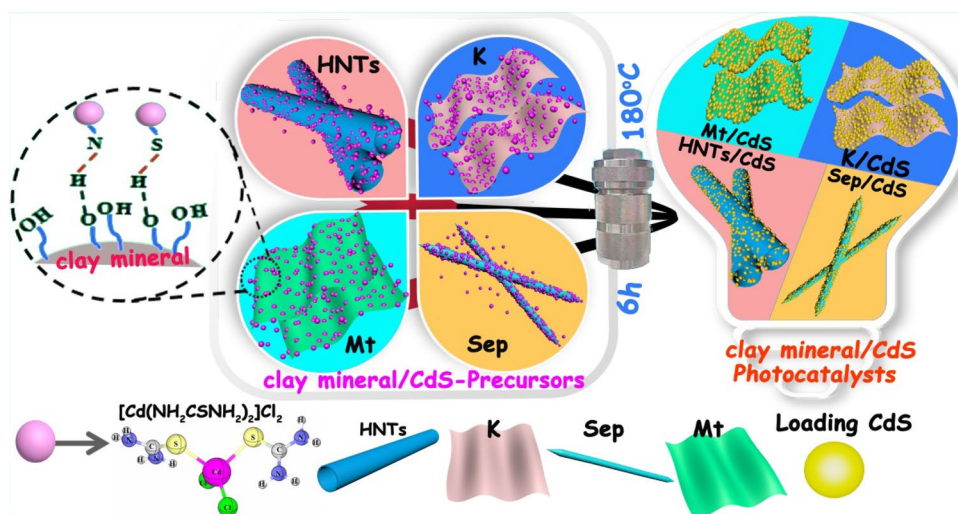
the nanocomposites particles. The concentration of CR at different time was measured by UV–Vis spectrophotometer at the wavelength of maximum absorbance (498 nm) for CR.

2.4 Characterizations

The compositions of clay minerals before and after acid-treatment were measured by X-ray fluorescence (XRF, JSM-5600LV, Japanese Electronic Optical Co., LTD, Japan) (Table S1). The Powder X-ray diffraction (XRD) patterns were recorded with X′Pert PRO diffractometer working at 40 kV and 30 mA and the 2θ scanning angle was in range of 3–80° at a step interval of about 0.167°. The Fourier-transform infrared (FTIR) spectra of samples were obtained on a Nicolet NEXUS FTIR in 4000–400 cm^{-1} region. The microstructure and size of the obtained nanocomposites were measured using a field emission transmission electron microscopy (TEM, JEM-1200 EX/S, JEOL, Tokyo, Japan), respectively. The Raman spectrum was performed for powder nanocomposites using a Horiva (Lab Ram HR-800) spectrometer. The color properties of all nanocomposites were in terms of the Commission Internationale de l'Eclairage (CIE) 1976 $L^*a^*b^*$ colorimetric method using a Color-Eye automatic differential colorimeter (X-Rite, Ci 7800). In the CIE $L^*a^*b^*$ system, L^* values signify color lightness between 0 (black) and 100 (white), a^* value is green (negative)/red (positive) axis, and b^* is the blue (negative)/yellow (positive). C^* (chroma) represents saturation of color, which was calculated according to which is defined as $C^* = [(a^*)^2 + (b^*)^2]^{1/2}$, and h^o stands for the hue angle ranging from 0° to 360° according to $h^o = \arctan(b^*/a^*)$. Besides, reflectance and UV–Vis spectra were also recorded with X-Rite, Ci 7800. The Brunauer–Emmett–Teller (BET) specific surface area was measured at 77 K using the surface area and porosity analyzer (Micromeritics, U.S.A).

Photoluminescence spectra (PL) were performed on an Edinburgh FL/FS900 spectrophotometer.

3 Results and discussion

3.1 Characterization of clay mineral/CdS nanocomposites

3.1.1 Optical and color analysis

Figure 2 presented digital photographs, UV–Vis diffuse reflectance spectra, absorption edge, E_g and color parameters of all as-prepared samples. As shown in their digital photographs, all samples presented jacinth (Fig. 2a), and the reflectance of all clay mineral/CdS nanocomposites decreased compared with CdS in the range of 600–750 nm (Fig. 2b, inset). For K/CdS samples, the magnitude of reduction was lowest (about 82%) while the reflectance of pure CdS samples was 84%. Moreover, all samples had the lowest reflectance in the range of about 360–500 nm, which signified largest absorbance at the same wavelength range. Although the shapes of five spectra were quite similar for clay mineral/CdS nanocomposites, they displayed different onset location and peak absorbance, revealing that the absorbance was affected by the types of clay minerals [25]. The Kubelka–munk plot results (Fig. 2b) demonstrated that incorporation of clay minerals led to a blue-shift or red-shift in the absorption edge of samples. Absorption edges of Mt/CdS and K/CdS red-shifted to 555 nm and 556 nm compared with that of pure CdS, respectively, while other samples blue-shifted to 524 nm, 533 nm, and 529 nm for Pal/CdS, Sep/CdS, and HNTs/CdS, respectively (Fig. 2c). Furthermore, the direct band gaps of all samples could be calculated according to the following equation:
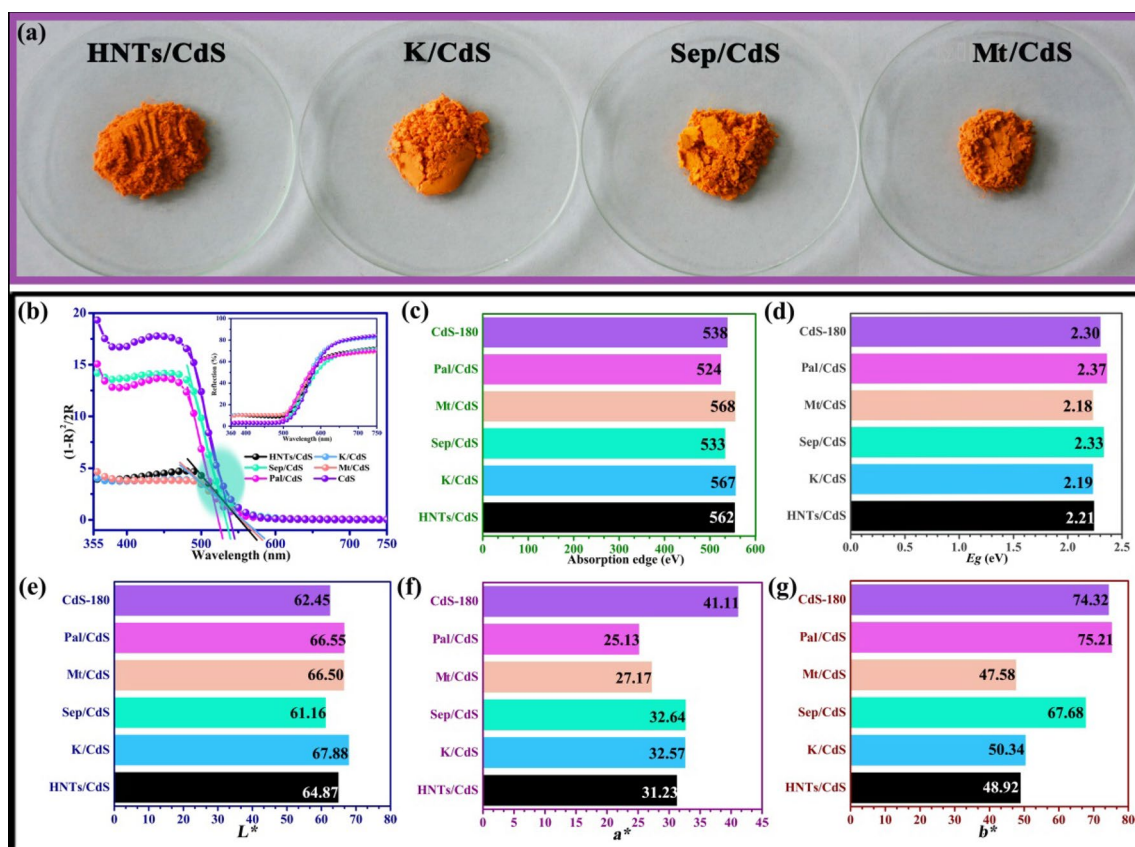
$$E_g = \frac{1240}{\lambda}$$

Fig. 2 **a** Digital photographs, **b** Kubelka–munk plot, inset: UV–Vis diffuse reflectance spectra, **c** absorption edge, **d** E_g, **e** L^*, **f** a^* and **g** b^* of clay mineral/CdS nanocomposites (Relevant data about CdS and Pal/CdS came from our earlier report [26])

where λ is the wavelength (nm) of the absorption edges in the spectra. As shown in Fig. 2d, the calculated E_g of clay mineral/CdS nanocomposites also presented the obvious differences, which might be due to the differences in the interface interaction between CdS nanoparticles and clay minerals [27].

In addition, it had been proven that the color parameters were closely related to E_g and optical performance of materials [28]. Therefore, the color properties of clay mineral/CdS nanocomposites also were characterized by CIE L^* a^* b^* system (Figs. 2, S1). Compared with pure CdS, clay mineral/CdS nanocomposites exhibited different color parameters. Among these color parameters, L^* values of clay mineral/CdS nanocomposites were above 60, while the a^* values were lower than that of CdS, suggesting the low red phase. The b^* values of clay mineral/CdS nanocomposites were also lower than pure CdS except for Pal/CdS sample. It was well-known that h^o of yellow color was in range of 70–105°, and h^o values of the as-prepared nanocomposites and pure CdS were between 57° and 70° except for Pal/CdS nanocomposites, which might be related to their high redness. Chromatic *CIE* coordinates of clay mineral/CdS nanocomposites and CdS also confirmed their color differences (Fig.

S1c). It suggested that incorporation of different clay minerals were capable of adjusting the color of clay mineral/CdS nanocomposites to some extent.

3.1.2 XRD

The XRD patterns of clay mineral/CdS nnaocomposites prepared using different clay minerals were performed to investigate the crystal phase and average particle size (Fig. 3, Table 1). For all samples, nine main diffraction peaks located at $2\theta = 24.93°$, 26.67°, 28.19°, 36.79°, 43.65°, 47.79°, 50.84°, 51.81°, and 52.80° corresponded to (100), (002), (101), (102), (110), (103), (200) and (201) planes, respectively, which were well matched the hexagonal wurtzite CdS structure of *P63mc* space group (JCPDS No. 41-1049) [29]. Meanwhile, some characteristic diffraction peaks of clay minerals were also observed in their XRD patterns (Fig. S2). With the help of Jade 6.0 by peak-fitting analyses, Delphi process and Debye–Scherrer [30] by major XRD peak of (101) plane of hexagonal CdS for all nanocomposites, crystallite sizes and lattice parameters, volumes were calculated and presented in Table 1. It was found that crystallite sizes of clay mineral/CdS nanocomposites ranged
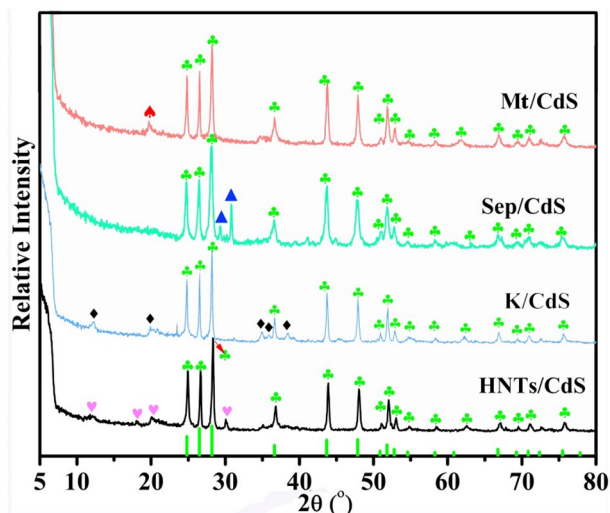
Fig. 3 XRD patterns of clay mineral/CdS nanocomposites

from 37 to 51 nm, which were smaller than pure CdS. It might be due to the fact that incorporation of clay minerals effectively prevented from the agglomeration of CdS nanoparticles. Furthermore, the lattice parameters and volumes of clay mineral/CdS nanocomposites changed slightly compared with that of the pure CdS with lattice constants of $a = b = 4.12551$ Å, $c = 6.70100$ Å and $V = 98.7815$ Å^3. Moreover, lattice parameters and volumes of clay mineral/CdS nanocomposites decreased in the order of Sep/CdS > K/CdS > Pal/CdS > Mt/CdS > HNTs/CdS > CdS. The change of unit cell for HNTs/CdS, Mt/CdS, K/CdS and Pal/CdS was slight, except for Sep/CdS. This might be attributed to the expansion of unit cell by the substitution of larger ions derived from Sep during hydrothermal reaction (such as

Ca^{2+}, see Table S2) [31]. Based on XRD results, it suggested that different clay mineral had different effects on the lattice of CdS crystal, which might be attributed to the differences in the nucleation and growth of the sulfide nanoparticles during the hydrothermal process [25, 32].

3.1.3 FT-IR and Raman spectra

The FTIR spectra of clay mineral/CdS nnaocomposites were presented in Fig. 4a. For all samples, the double peaks around 3690 cm^{-1} and 3620 cm^{-1} were assigned to the stretching vibrations of hydroxyl –OH groups on the outer-surface of clay minerals [11, 33]. The bands around 3440 cm^{-1} and 1630 cm^{-1} were attributed to the stretching vibrations of the hydroxyl groups of water and the bending vibrations of adsorbed water molecules between layers of clay minerals, respectively [18]. Meanwhile, the absorption bands near 1080 cm^{-1}, 1030 cm^{-1} and 910 cm^{-1} were attributed to stretching vibration of Si-O groups and the vibration of inner Al-OH groups of clay minerals. The three bands (791 cm^{-1}, 750 cm^{-1} and 690 cm^{-1}) and other three bands (around 545 cm^{-1}, 470 cm^{-1} and 430 cm^{-1}) were mainly assigned to the vibration of O–Al–OH and Si–O–Al, respectively. The weak characteristic absorption bands around 1385 cm^{-1} and 600–670 cm^{-1} were ascribed to the vibration of Cd–S bond [34, 35]. In the FT-IR spectra of clay mineral/CdS nanocomposites, some peaks of CdS in Mt/CdS nanocomposites were weak in contrast with Mt due to weak absorption of CdS in the IR region. Based on results of XRD and FT-IR, it revealed that the prepared nanocomposites were composed of clay minerals and CdS.

Figure 4b showed the typical Raman spectra of clay mineral/CdS to further investigate the effect of clay minerals
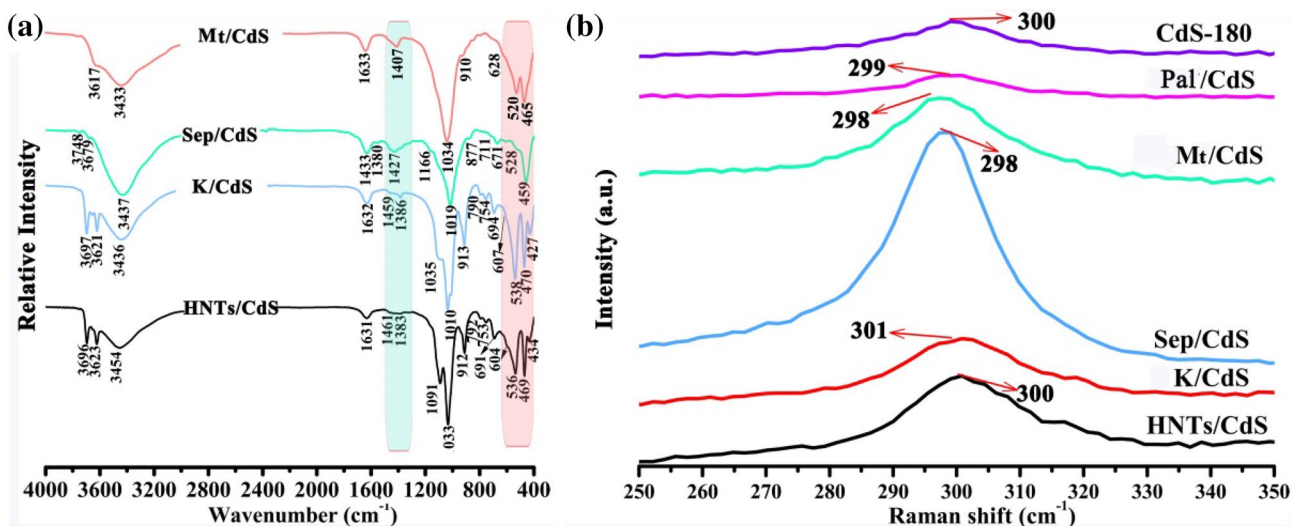

Fig. 4 **a** FT-IR spectra and **b** Raman spectra of clay mineral/CdS nanocomposites

on optical properties of CdS nanoparticles. The prominent Raman peak around 300 cm^{-1} was attributed to first order scattering of the longitudinal optical (*1LO*), which was confirmed the hexagonal wurtzite structure of CdS in clay mineral/CdS nanocomposites. Moreover, the asymmetric *1LO* peak implied the presence of the defects in the crystalline structure of clay mineral/CdS nanocomposites [36]. By contrast, the frequency of the *1LO* peak location of clay mineral/CdS nanocomposites shifted to 304 cm^{-1} (HNTs/CdS), 301 cm^{-1} (K/CdS), 298 cm^{-1} (Sep/CdS), 298 cm^{-1} (Mt/CdS) and 299 cm^{-1} (Pal/CdS) compared with that of pure CdS (300 cm^{-1}), which were mainly due to the grain size effect after incorporating of different clay minerals. It suggested the differences in sizes of CdS nanoparticles from clay mineral/CdS nanocomposites [37].

3.1.4 TEM

In order to visualize the morphologies of clay mineral/CdS nanocomposites, TEM characterization was conducted using HNTs/CdS nanocomposites as an example (Fig. 5). It was observed that the exterior and inner diameters of pristine HNTs was about 40–75 nm nm and 10–20 nm, respectively (Fig. 5a). As shown in Fig. 5b, HNTs/CdS nanocomposite presented a typical tubular structure loaded with spherical nanoparticles with size of 8–15 nm. In addition, the selected area electron diffraction (SAED) patterns were also indexed to a hexagonal wurtzite structure for CdS in HNTs/CdS nanocomposites, in which the diffraction dots were corresponded to the (104), (102), (110), (103) and (202) places CdS, respectively (Fig. 5c).

3.1.5 BET surface area

Table 1 listed the BET surface area of the prepared clay mineral/CdS nanocomposites. The surface areas for HNTs/CdS, K/CdS, Sep/CdS, Mt/CdS, Pal/CdS and CdS were 45.2549 m^2/g, 10.8548 m^2/g, 16.9579 m^2/g, 65.5556 m^2/g, 97.0834 m^2/g and 7.6719 m^2/g, respectively. It was obvious

that specific surface areas of clay mineral/CdS nanocomposites were higher than CdS, especially incorporation of HNTs, Mt and Pal. It suggested that incorporation of clay minerals was in favor of improving the aggregation of CdS nanoparticles, which was crucial to enhance the photocatalytic activity of CdS.

3.2 Photocatalytic properties of clay mineral/CdS nanocomposites

3.2.1 Photocatalytic degradation of CR

CR (Fig. S3) [1-naphthalenesulfonic acid, 3,3′-(4,40-biphenylenebis(azoz) bis (4-amino) disodium salt] is a linear symmetrical molecule and belongs to carcinogenic anionic dye [38]. To date, it has been widely used in a number of industries such as cosmetic manufacturing, textile, paper, leather, even rubber and plastic fields [39]. The random discharge of wastewater containing CR into aquatic system would cause multitude damage to environment due to its high toxic. Thus, photocatalytic degradation properties of the as-prepared clay mineral/CdS nanocomposites to CR were evaluated at room temperature. As shown in Fig. 6, the degradation percentage increased gradually with increasing the visible light irradiation time for clay mineral/CdS samples, but the distinct differences in the degradation percentage were observed for different samples.

Figure 6a displayed the plot of C/C_0 of CR *vs.* irradiation time t, the concentration of CR decreased to 5.7%, 6.5% and 3.0% after visible light irradiation for 30 min, respectively, revealing that the degradation of CR could reach 94.3%, 93.5% and 97.0% for HNTs/CdS, Sep/CdS and Pal/CdS samples. It also could be observed that the fading of liquid supernatants was noticeable when the irradiation time was up to 30 min (Figs. 6d inset, S4). As irradiation time continuously increased to 80 min, the concentration of CR slightly decreased to 2.3%, 3.0% and 2.4%, respectively. However, the concentration of CR exceeded 5.0%, even reached 17.8%
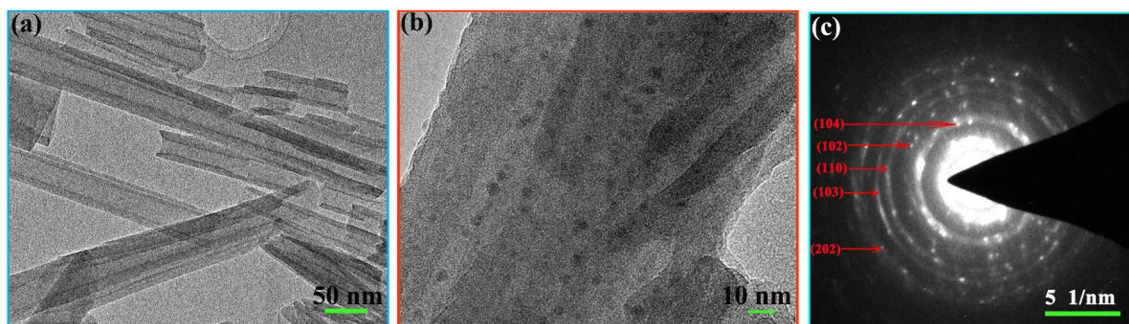
Fig. 5 TEM images of **a** HNTs and **b** HNTs/CdS. **c** SAED patterns of HNTs/CdS nanocomposites

Fig. 6 Photocatalytic activity of clay mineral/CdS nanocomposites: **a** plot of (C/C_0) versus t; **b** plot of $-\ln(C/C_0)$ versus t; **c** absorption spectra of clay mineral/CdS nanocomposites under visible light irradiation for 80 min; **d** UV–vis spectra of CR solution after addition of HNTs/CdS nanocomposites. Inset: photographs of CR solution at different time after addition of HNTs/CdS nanocomposites
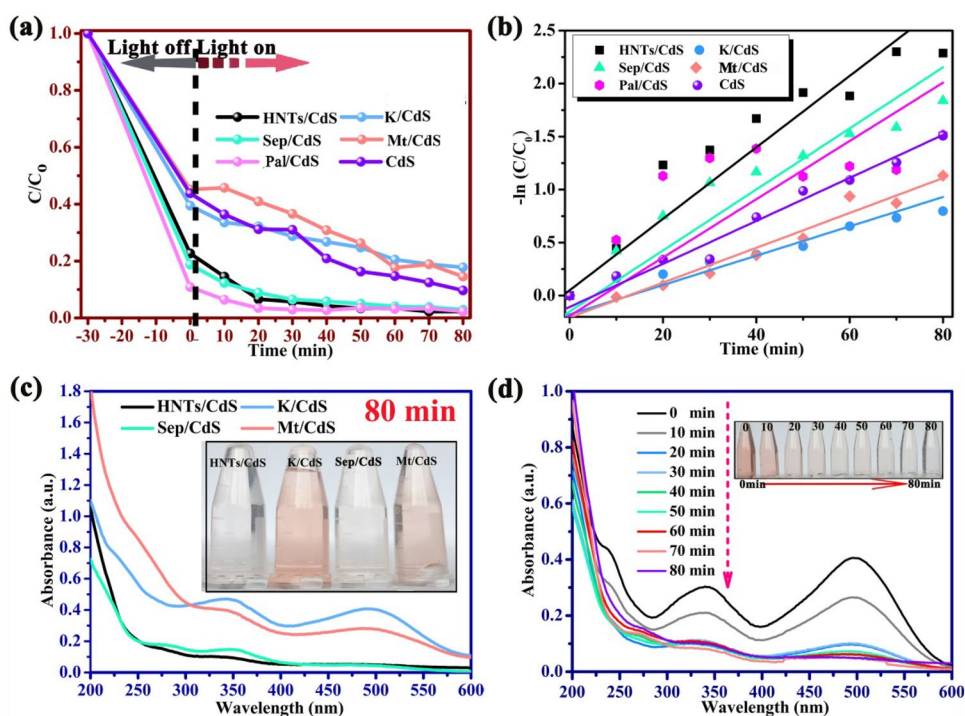
for K/CdS and 14.6% for Mt/CdS, which were higher than that of pure CdS (9.7%).

To statistically compare their photocatalytic efficiency, the pseudo-first-order model ($\ln(C/C_0) = -k_{app} \times t$) was used to quantitatively evaluate, and the rate constant k_{app} values were listed in Table S1. The order of k_{app} values for samples was HNTs/CdS > Sep/CdS > Pal/CdS > Mt/CdS > K/CdS in turn. It suggested that k_{app} values were in accordance with photocatalytic activities of these samples (Fig. 6b), and the photocatalytic activities of Mt/CdS and K/CdS samples were inferior to that of pure CdS. In other word, the samples prepared using one-dimensional clay minerals showed higher photocatalytic activity for CR than that of two-dimensional ones, which might be related to the different formation mechanism of samples. The introduction of one-dimensional clay mineral could effectively induce the uniform encapsulation of nanoparticles on the surface of clay minerals, preventing the formation of free aggregates of nanoparticles [40]. However, two-dimensional clay minerals could be well intercalated and encapsulated by the generated nanoparticles [41]. Therefore, the loading of nanoparticles on the surface of clay mineral with one-dimensional structure were easy to expose in the reaction system than that of two-dimensional clay minerals, which might provide more active site for photocatalytic reaction. The incorporation of clay minerals could enhance the photocatalytic properties of the photocatalyst, and improve the stability and limit the size of CdS due to its unique characteristics.

In addition, zeta potentials of clay mineral/CdS photocatalysts presented negative value (Table 1), and hence the

disappearance of CR color was not attributed to electrostatic attraction of nanocomposite and CR to explain the adsorption process. In fact, the formed aromatic pi-cloud between the CR dye in hydrogen bonding and silanol OH groups of Halalso were beneficial to remove CR dye by the nanocomposite [42]. In order to track the photocatalytic degradation process, the comparative experiments were also performed. In a typical procedure, 30 mg of HNTs/CdS nanocomposites were firstly added into 30 ppm of CR solution, and then the reaction was conducted under two conditions to assess photocatalytic and adsorption process, respectively. The one was under black light for 30 min and visible light irradiation for 80 min; the other was under black light for 110 min. After these processes, the precipitates were separated by centrifugation, and subsequently washed with water several times before being dried at 60 °C for 24 h. At last, the desorption experiments from the obtained precipitates were carried out by adding 10 mL ethanol and shocked 12 h at 25 °C. The concentration of CR in supernatant was measured by UV–Vis spectrophotometer. As shown in Fig. S5a, b, the photocatalytic degradation and adsorption of CR during the visible light irradiation time were obviously observed, and the adsorption rate on HNTs/CdS nanocomposite reached to 44% under dark conditions, which was about two times of that of CdS nanoparticles (22% only). Based on above results, it was implied that the color disappearance of CR after introduction of the samples were mainly ascribed to synergistic effect of photocatalytic degradation and adsorption of clay mineral/CdS nanocomposites in the visible light irradiation time. This conclusion also might be proved by

UV–Vis spectra and photographs of CR solution for HNTs/CdS nanocomposite under visible light for 0 min and dark light for 80 min, respectively (Figs. 6c, S6).

Meanwhile, it had been confirmed that electron and O_2 played a primary role in the photodegradation of dye. Due to more positive potential of the photogenerated holes than VB potential of CdS, the photogenerated holes of CdS could be not oxidize directly OH^- and H_2O [43]. Meanwhile, combined with the previous studies [44–48], a schematic illustration was proposed to clearly elucidate the probable photocatalytic reaction mechanism for clay mineral/CdS nanocomposite (Fig. 7). The photocatalytic degradation for CR dyes in this system was initiated by the photoexcitation of clay mineral/CdS nanocomposites. These excited electrons ($e^-_{(CB)}$) in conduction band induced oxygen to produce superoxide radical ($O_2^{\bullet}$). Subsequently, these superoxide radicals further took part in the dye degradation. Ultimately, CR was mineralized partially or completely into CO_2 and H_2O. In a word, incorporation of clay minerals prevented from the electrochemical corrosion of CdS, and different clay minerals also played different photocatalytic effects for CR degradation.

3.2.2 Compare with photocatalytic activity of clay mineral/CdS nanocomposites

Based on above results, it was found that the as-prepared nanocomposites derived from one-dimensional clay minerals including tubular, fibrous and rod-like presented higher photocatalytic activity for CR degradation than that of two-dimensional lamellar ones in the visible light. Hence, it revealed that the primary factor affecting photocatalytic activity of clay mineral/CdS nanocomposites might be the morphologies of clay minerals. Moreover, the reported two-dimensional clay mineral/CdS nanocomposites paid more attention to synthesis and interfacial feature, but it was few reported for the photocatalytic activity in the visible light [25], which might be due to the weak photocatalytic activity.

Compared with two-dimensional clay minerals, one-dimensional clay minerals might be in favor of increasing activity of CdS due to the different formation mechanism [49, 50]. In addition, E_g values of two-dimensional clay mineral/CdS nanocomposites were lower than pure CdS (2.19 eV) and clay mineral/CdS nanocomposites with one-dimensional structure (2.18 eV), which might much more easier to cause recombination of electron hole pairs of semiconductor compared with that of pure CdS (Fig. S7) and one-dimensional clay mineral/CdS nanocomposites. According to the early reports [43], the change of E_g of clay mineral/CdS nanocomposites was attributed to the interaction between CdS and clay minerals, rather than a quantum confinement effect.

In the case of clay mineral/CdS nanocomposites prepared using same dimensional clay mineral, the lower E_g of clay mineral/CdS nanocomposites, the better the photocatalytic activity. In brief, photocatalytic activity and the stability of clay mineral/CdS nanocomposites were affected by the morphologies of clay mineral and E_g, which might be due to the difference in the grain size of CdS nanoparticles in clay mineral/CdS nanocomposites, optical properties, morphologies of nanocomposites and chemical composition of clay minerals.

4 Conclusions

In summary, a series of clay mineral/CdS nanocomposites were successfully synthesized using five types of clay minerals by a one-step hydrothermal method. The photocatalytic experiments indicated clay mineral/CdS photocatalysts based on one-dimensional clay minerals exhibited higher photocatalytic activity for degradation of CR than that of two-dimensional ones. The photocatalytic activity and the stability of clay mineral/CdS nanocomposites were affected by the morphologies of clay mineral and E_g of the as-prepared nanocomposites. What' more, it is expected to adjust

Fig. 7 Schematic diagram for the photodegradation of CR using HNTs/CdS as an example
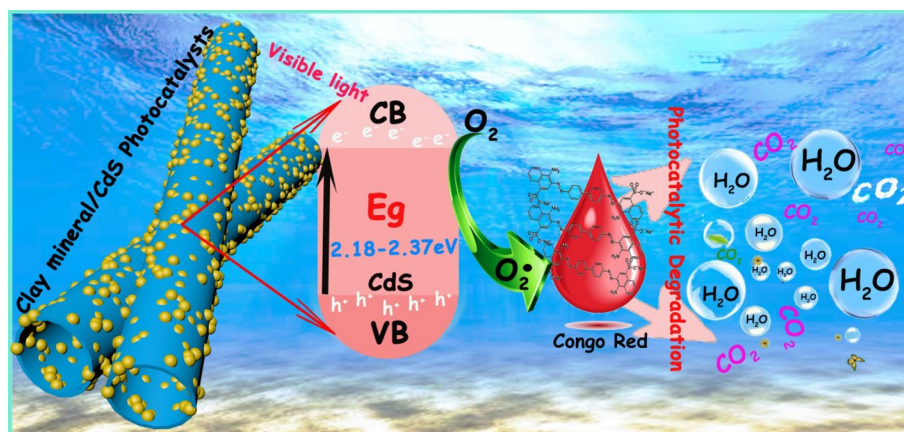
the color and photocatalytic properties of CdS by incorporation of different clay minerals.

References

1. Y. Shi, K. Zhou, B. Wang et al., Ternary graphene-CoFe$_2$O$_4$/CdS nanohybrids: preparation and application as recyclable photocatalysts. J. Mater. Chem. A **2**, 535–544 (2014)

2. X. Li, W. Zhang, N. Liu et al., Superwetting copper meshes based on self-organized robust CuO nanorods: efficient water purification for in situ oil removal and visible light photodegradation. Nanoscale **10**, 4561–4569 (2018)

3. L. Zhang, T. Wang, H. Wang et al., Graphene@poly(m-phenylenediamine) hydrogel fabricated by a facile post-synthesis assembly strategy. Chem. Commun. **49**, 9974–9976 (2013)

4. X. Ma, P. Chen, M. Zhou et al., Tight ultrafiltration ceramic membrane for separation of dyes and mixed salts (both NaCl/Na$_2$SO$_4$) in textile wastewater treatment. Ind. Eng. Chem. Res. **56**, 7070–7079 (2017)

5. K. Hedayati, S. Azarakhsh, J. Saffari et al., Magnetic and photocatalyst CoFe$_2$O$_4$–CdS nanocomposites: simple preparation of Ni, Co, Zn or Ag-doped CdS nanoparticles. J. Mater. Sci. **28**, 5472–5484 (2017)

6. K.P. Sonu, B.V.V.S.P. Kumar, S.J. George et al., Simple and facile approach to create charge reversible pores via hydrophobic anchoring of ionic amphiphiles. ACS Appl. Mater. Interfaces **9**, 9136–9142 (2017)

7. F.L.Y. Lam, X. Hu, pH-insensitive bimetallic catalyst for the abatement of dye pollutants by photo-fenton oxidation. Ind. Eng. Chem. Res. **52**, 6639–6646 (2013)

8. A. Christodoulakis, M. Machli, A.A. Lemonidou et al., Molecular structure and reactivity of vanadia-based catalysts for propane oxidative dehydrogenation studied by in situ Raman spectroscopy and catalytic activity measurements. J. Catal. **222**, 293–306 (2004)

9. S. Rondiya, A. Rokade, P. Sharma et al., CZTS/CdS: interface properties and band alignment study towards photovoltaic applications. J. Mater. Sci. **29**, 4201–4210 (2018)

10. J.X. Lv, Z.M. Zhang, J. Wang et al., In situ synthesis of CdS/Graphdiyne heterojunction for enhanced photocatalytic activity of hydrogen production. ACS Appl. Mater Interfaces **11**, 2655–2661 (2018)

11. W. Xing, L. Ni, P. Huo, Z. Lu et al., Preparation high photocatalytic activity of CdS/halloysite nanotubes (HNTs) nanocomposites with hydrothermal method. Appl. Surf. Sci. **259**, 698–704 (2012)

12. Q. Wang, J. Lian, Q. Ma et al., Preparation of carbon spheres supported CdS photocatalyst for enhancement its photocatalytic H$_2$ evolution. Catal. Today **281**, 662–668 (2017)

13. H. Gao, Z. Mo, R. Guo et al., Formation of snowflake-like CdS/reduced graphene oxide composite for efficient photocatalytic organic dye degradation. J. Mater. Sci. **29**, 5944–5953 (2018)

14. H. Chen, S. Cao, J. Yao et al., Fabrication of Ag nanowires-CdS-Au photocatalyst and its excellent visible light photocatalytic activity: the role of synergetic electron transfer. J. Taiwan. Inst. Chem. E. **71**, 189–196 (2017)

15. R. Peng, C.M. Wu, J. Baltrusaitis et al., Solar hydrogen generation over CdS incorporated in Ti-MCM-48 mesoporous materials under visible light illumination. Int. J. Hydrogen Energy **41**, 4106–4119 (2016)

16. Z. Han, Q. Yang, J. Shi et al., Well-dispersed cadmium sulfide prepared in the presence of laponite by microwave irradiation. Solid State Sci. **10**, 563–568 (2008)

17. F. Zhou, D. Chen, B. Cui et al., Synthesis and characterization of CdS/TiO$_2$-montmorillonite nanocomposite with enhanced visible-light absorption. J. Spectrosc. (2014). https://doi.org/10.1155/2014/961230

18. H. Boukhatem, L. Djouadi, N. Abdelaziz et al., Synthesis, characterization and photocatalytic activity of CdS-montmorillonite nanocomposites. Appl. Clay Sci. **72**, 44–48 (2013)

19. X. Li, L. Fu, J. Ouyang et al., Microwave-assisted synthesis and interfacial features of CdS/kaolinite nanocomposite. Colloid Surf. A **443**, 72–79 (2014)

20. V. Štengl, D. Popelková, T.M. Grygar, Composite pigments based on surface coated kaolin and metakaolin. Appl. Clay Sci. **101**, 149–158 (2014)

21. V.A. Vinokurov, A.V. Stavitskaya, E.V. Ivanov et al., Halloysite nanoclay based CdS formulations with high catalytic activity in hydrogen evolution reaction under visible light irradiation. ACS Sustain. Chem. Eng. **5**, 11316–11323 (2017)

22. J. Zhang, R. He, X. Liu, Efficient visible light driven photocatalytic hydrogen production from water using attapulgite clay sensitized by CdS nanoparticles. Nanotechnology **24**, 505401 (2013)

23. D. Chen, Y. Du, H. Zhu et al., Synthesis and characterization of a microfibrous TiO$_2$-CdS/palygorskite nanostructured material with enhanced visible-light photocatalytic activity. Appl. Clay Sci. **87**, 285–291 (2014)

24. J. Xiao, T. Peng, K. Dai et al., Hydrothermal synthesis, characterization and its photoactivity of CdS/rectorite nanocomposites. J. Solid State Chem. **180**, 3188–3195 (2007)

25. Z. Han, H. Zhu, K.R. Ratinac et al., Nanocomposites of layered clays and cadmium sulfide: Similarities and differences in formation, structure and properties. Microporous Mesoporous Mater. **108**, 168–182 (2008)

26. X. Wang, B. Mu, X. An et al., Insights into the relationship between the color and photocatalytic property of attapulgite/CdS nanocomposites. Appl. Surf. Sci. **439**, 202–212 (2018)

27. D. Kandi, S. Martha, A. Thirumurugan et al., Modification of BiOI microplates with CdS QDs for enhancing stability, optical property, electronic behavior toward Rhodamine B decolorization, and photocatalytic hydrogen evolution. J. Phys. Chem. C **121**, 4834–4849 (2017)

28. K. Nasau, The causes of color. Sci. Am. **243**, 124–154 (1980)

29. S. Ma, Y. Deng, J. Xie et al., Noble-metal-free Ni$_3$C cocatalysts decorated CdS nanosheets for high-efficiency visible-light-driven photocatalytic H$_2$ evolution. Appl. Catal. B-Environ. **227**, 218–228 (2018)

30. J. Zhao, K. Ge, L. Zhao et al., Enhanced photocatalytic properties of CdS -decorated BiPO$_4$ heterogeneous semiconductor catalyst under UV-light irradiation. J. Alloy. Compd. **729**, 189–197 (2017)

31. C. Singh, A. Goyal, R. Malik et al., Envisioning the attachment of CdS nanoparticles on the surface of MFe$_2$O$_4$ (M = Zn, Co and Ni) nanocubes: analysis of structural, optical, magnetic and photocatalytic properties. J. Alloy Compd. **695**, 351–363 (2017)

32. D. Kashchiev, G.M. Van Rosmalen, Review: nucleation in solutions revisited. Cryst. Res. Technol. **38**, 555–574 (2010)

33. U.A. Khan, J. Liu, J. Pan et al., Fabrication of floating CdS/EP photocatalyst by facile liquid phase deposition for highly efficient degradation of Rhodamine B (RhB) under visible light irradiation. Mater. Sci. Semicond. Proc. **83**, 201–210 (2018)

34. R. Wang, J. Yan, M. Zu et al., Facile synthesis of interlocking g-C$_3$N$_4$/CdS photoanode for stable photoelectrochemical hydrogen production. Electrochim. Acta **279**, 74–83 (2018)

35. J. Fu, B. Chang, Y. Tian et al., Novel C$_3$N$_4$-CdS composite photocatalysts with organic–inorganic heterojunctions: in situ synthesis, exceptional activity, high stability and photocatalytic mechanism. J. Mater. Chem. A **1**, 3083–3090 (2013)

36. P. Chawla, S.P. Lochab, N. Singh, Photoluminescence, thermoluminescence and Raman studies of CdS nanocrystalline phosphor. J. Alloy Compd. **492**, 662–666 (2010)

37. E. Rani, A. A.Ingale, A.K. Sinha, Interaction between CdS nanocrystals and PVP leading to co-operative growth of CdS-PVP nanocomposites: a Raman and AFM mapping study. J. Alloy Compd. **729**, 597–602 (2017)

38. R. Arunadevi, B. Kavitha, M. Rajarajan et al., Investigation of the drastic improvement of photocatalytic degradation of Congo red by monoclinic Cd, Ba-CuO nanoparticles and its antimicrobial activities. Surf. Interfaces **10**, 32–44 (2018)

39. V.A. Sakkas, M.A. Islam, C. Stalikas et al., Photocatalytic degradation using design of experiments: a review and example of the Congo red degradation. J. Hazard. Mater. **175**, 33–44 (2010)

40. B. Mu, A. Wang, One-pot fabrication of multifunctional superparamagnetic attapulgite/Fe$_3$O$_4$/polyaniline nanocomposites served as adsorbent and catalyst support. J. Mater. Chem. A **3**, 281–289 (2015)

41. B. Mu, J. Tang, L. Zhang et al., Preparation, characterization and application on dye adsorption of a well-defined two-dimensional superparamagnetic clay/polyaniline/Fe$_3$O$_4$ nanocomposite. Appl. Clay Sci. **132–133**, 7–16 (2016)

42. F. Ferrarini, L.R. Bonetto, J.S. Crespo et al., Removal of Congo red dye from aqueous solutions using a halloysite-magnetite-based composite. Water Sci. Technol. **73**, 2132–2142 (2016)

43. D. Jiang, Z. Liu, L. Fu et al., Efficient nanoclay-based composite photocatalyst: the role of nanoclay in photogenerated charge separation. J. Phys. Chem. C **122**, 25900–25908 (2018)

44. H. Hu, M. Wang, C. Deng et al., Satellite-like CdS nanoparticles anchoring onto porous NiO nanoplates for enhanced visible-light photocatalytic properties. Mater. Lett. **224**, 75–77 (2018)

45. Z. Yu, B. Yin, F. Qu et al., Synthesis of self-assembled CdS nanospheres and their photocatalytic activities by photodegradation of organic dye molecules. Chem. Eng. J. **258**, 203–209 (2014)

46. I. Ullah, A. Haider, N. Khalid et al., Tuning the band gap of TiO$_2$ by tungsten doping for efficient UV and visible photodegradation of Congo red dye. Spectrochim. Acta A **204**, 150–157 (2018)

47. L. Zou, X. Wang, X. Xu et al., Reduced graphene oxide wrapped CdS composites with enhanced photocatalytic performance and high stability. Ceram. Int. **42**, 372–378 (2016)

48. A. Khan, R. Zia, M. Rehman et al., CdS nanocapsules and nanospheres as efficient solar light-driven photocatalysts for degradation of Congo red dye. Inorg. Chem. Commun. **72**, 33–41 (2016)

49. A. Mishra, A. Mehta, S. Basu, Clay supported TiO$_2$ nanoparticles for photocatalytic degradation of environmental pollutants: A review. J Environ. Chem. Eng. **6**, 6088–6107 (2018)

50. D. Kibanova, M. Trejo, H. Destaillats, J. Cervini-Silva, Synthesis of hectorite-TiO$_2$ and kaolinite-TiO$_2$ nanocomposites with photocatalytic activity for the degradation of model air pollutants. Appl. Clay Sci. **42**, 563–568 (2009)